Eur. Phys. J. Special Topics **208**, 259–274 (2012)

DOI: 10.1140/epjst/e2012-01623-2

THE EUROPEAN PHYSICAL JOURNAL SPECIAL TOPICS

Review

Quantitative anomalous small-angle X-ray scattering – The determination of chemical concentrations in nano-scaled phases

G. Goerigk[1,a], K. Huber[2], N. Mattern[3], and D.L. Williamson[4]

[1] Institute of Soft Matter and Functional Materials, Helmholtz-Zentrum Berlin, Germany
[2] Universität Paderborn, Fakultät für Naturwissenschaften, Department Chemie, Germany
[3] Leibniz-Institute IFW Dresden, Institute for Complex Materials, Germany
[4] Colorado School of Mines, USA

Received 15 October 2011 / Received in final form 23 March 2012
Published online 15 June 2012

Abstract. In the last years Anomalous Small-Angle X-ray Scattering became a precise quantitative method resolving scattering contributions two or three orders of magnitude smaller compared to the overall small-angle scattering, which are related to the so-called pure-resonant scattering contribution. Additionally to the structural information precise quantitative information about the different constituents of multi-component systems like the fraction of a chemical component implemented into the materials nanostructures are obtained from these scattering contributions. The application of the Gauss elimination algorithm to the vector equation established by ASAXS measurements at three X-ray energies is demonstrated for three examples from chemistry and solid state physics. All examples deal with the quantitative analysis of the Resonant Invariant (RI-analysis). From the integrals of the pure-resonant scattering contribution the chemical concentrations in nano-scaled phases are determined. In one example the correlated analysis of the Resonant Invariant and the Non-resonant Invariant (NI-analysis) is employed.

1 Introduction

Anomalous Small-Angle X-ray Scattering (ASAXS) is an excellent tool for the chemical selective structural analysis of multi-component systems. In the last three decades numerous ASAXS studies on alloys, ceramics, magnetic systems, catalysts, semiconductors, glasses, polymers, membranes and other soft matter systems have been performed. A review can be found under [1]. These materials show strong differences, when analyzed by ASAXS. For instance metal nanoparticles prepared on porous support structures show a strong small-angle X-ray scattering predominantly related to the small-angle X-ray scattering of the pores, while the scattering of the metal nanoparticles is a minor contribution due to their small volume fraction [2,3].

[a] e-mail: guenter.goerigk@helmholtz-berlin.de

Glasses and alloys especially when dealing with metallic glasses show a different behaviour i.e. only a weak SAXS signal is originating from small concentration fluctuations of the different constituents [4,5]. The situation is similar for diluted chemical solutions like polyelectrolytes surrounded by counter ions, where the overall SAXS signal is weak due to the dilution and small changes occur, which are related to specifically interacting counter ions [6].

In the course of this paper the quantitative chemical analysis of nano-scaled phases in three different systems is addressed: (1) the conformation of macromolecules under the influence of counter ions in a highly diluted aqueous solution (2) the inhomogeneous distribution of Germanium and Hydrogen in semiconductor alloys and (3) the spinodal decomposition in metallic Ni-Nb-Y glasses. The different systems have in common a high degree of dilution and/or homogeneity and thus are weak scattering systems. The related scientific problems cannot be addressed by a classical Small-Angle X-ray Scattering (SAXS) experiment, because the specific scattering contributions of the different chemical components need to be separated. The Gauss elimination algorithm is applied to the vector equation introduced by ASAXS measurements performed at in minimum three energies.

Precise SAXS measurements in the resolution regime $10^{-3} < \Delta I/I < 10^{-2}$ (separated scattering with respect to the overall scattering) have been performed. Precise corrections (background, sensitivity, transmission, normalization, dead time correction, subtraction of solvent scattering...) and the calibration of the scattering curves into absolute units are mandatory and have to meet these accuracy requirements (i.e. should be better by one order in magnitude). In order to meet these accuracies the measurements followed the JUSIFA standard procedures as following. The detector sensitivity of the 2d-MWPC-detector at the different energy ranges was obtained by measurement of the fluorescence of suitable foils (i.e. Cu-, Se-, Zr- and Mo-foils with K-α lines at 8, 11.2, 15.8 and 17.5 keV). The error of these sensitivity measurements due to the counting statistics was better 0.5% for each pixel). Due to integration of the scattering curves the propagating error is smaller by one to two orders of magnitude. Within an energy range of 2 keV the sensitivity of the MWPC-detector does not changed signitficantly and thus can be used for corrections within an ASAXS sequence in the related energy ranges. Transmission measurements were preformed with a precision of 10^{-4} using a special (windowless) photodiode (Hamamatsu S2387-1010N). Corrections of the sensitivity of the diode are not necessary because it cancels out in the transmission measurement. The dead-time correction of the MWPC-detector was measured for each exposure and corrected for in the data reduction. The normalization of the scattering pattern was performed by measurements of the primary photon flux with a Sodium-Iodine scintillation counter with an accuracy of better than 10^{-4}. The background scattering and scattering from the solvent (respective substrate) was measured with the same exposure times like the samples and subtracted from the sample scattering. The scattering curves of all sample measurements (including the solvent and substrate measurements) have been calibrated into macroscopic scattering cross section in units of cross-section per unit volume $[cm^2/cm^3] = [cm^{-1}]$ by repeating the calibration measurements (with the JUSIFA glassy carbon standards) up to 20 times and averaging over these measurements. The errors have been calculated via error propagation law from the statistical errors of the photon counts of all contributing measurements (i.e. measurements of sample and solvent or substrate scattering, sensitivity, background...).

From the pure-resonant scattering contribution and the subsequent analysis of the Resonant Invariant (RI) the chemical concentrations in the related nano-phases were deduced. Additionally from the separated pure-resonant scattering the contributions of the other chemical components entering the so-called mixed-resonant and

non-resonant scattering can be reconstructed. All measurements were carried out at the JUSIFA beam line at HASYLAB, DESY Hamburg [7,8].

2 Anomalous small-angle X-ray scattering

The remarkable possibilities of the ASAXS technique are based on the energy dependence of the atomic scattering factors giving selective access to the specific SAXS contributions of nano-scaled phases, which are built up by different chemical constituents in composites like for instance alloys or chemical solutions. In general the atomic scattering factors are energy dependent complex quantities:

$$f_Z(E) = f_{0,Z} + f'_Z(E) + if''_Z(E), \tag{1}$$

where Z represents the atomic number. When performing ASAXS measurements on multi-component systems in the vicinity of the absorption edge of one of the sample constituents the scattering amplitude is:

$$A(\vec{q},E) = \int\limits_{V_p} \Delta\rho_0(\vec{r}) \cdot \exp(-i\vec{q}\vec{r})d^3r + \int\limits_{V_p} \Delta\rho_R(\vec{r},E) \cdot \exp(-i\vec{q}\vec{r})d^3r, \tag{2}$$

where q is the magnitude of the scattering vector [$= (4\pi/\lambda)\sin\Theta$], 2Θ is the scattering angle, λ the X-ray wavelength and V_p is the irradiated sample volume. $\Delta\rho_0, \Delta\rho_R$ are the differences of electron densities of the non-resonant and the resonant scattering atoms,

$$\begin{aligned} \Delta\rho_0(\vec{r}) &= \Delta f_0 \cdot u(\vec{r}) = (f_0 - \rho_m V_0) \cdot u(\vec{r}) \\ \Delta\rho_R(\vec{r},E) &= \Delta f_R(E) \cdot v(\vec{r}) = ((f_{0,R} - \rho_m V_R) + f'_R(E) + if''_R(E)) \cdot v(\vec{r}) \end{aligned} \tag{3}$$

calculated from the electron density, ρ_m, and the atomic (molecular) volumes V_0 and V_R, respectively. In the two cases of an alloy or a diluted solution ρ_m is the electron density of the entire alloy or of the solvent respectively. The volume V_0 represents the atomic (molecular) volume of the non-resonant scattering atoms or molecules for instance the volume of polymer chains in the case of the diluted solutions. V_R corresponds to the atomic volumes of the resonant scattering atoms. The functions $u(\vec{r}), v(\vec{r})$ are the number densities of the non-resonant and the resonant scattering atoms, respectively and represent their spatial distribution in the sample. The atomic (molecular) scattering factor, $f_0(E) \approx$ const, is nearly energy independent, while the atomic scattering factor, $f_R(E) = f_{0,R} + f'_R(E) + if''_R(E)$, shows strong variation with the energy in the vicinity of the absorption edge of the resonant scattering atoms due to the so-called anomalous dispersion corrections $f'_R(E), f''_R(E)$. Calculating the scattering intensity $I(\vec{q},E) = |A(\vec{q},E)|^2 = A(\vec{q},E)\cdot A^*(\vec{q},E)$ by means of Eqs. (2)–(3) and averaging over all orientations yields a sum of three contributions $I(q,E) = S_0(q) + S_{0R}(q) + S_R(q)$, with the convolution integrals [9]:

$$\begin{aligned} S_0(q) &= \Delta f_0^2 \iint\limits_{V_p} u(\vec{r})u(\vec{r}')\frac{\sin(q\,|\vec{r}-\vec{r}'|)}{q\,|\vec{r}-\vec{r}'|}d^3r d^3r' = \Delta f_0^2\,|A_0(q)|^2\,, \\ S_{0R}(q,E) &= 2\Delta f_0 \cdot (f_{0,R} - \rho_m V_R + f'_R(E)) \iint\limits_{V_p} u(\vec{r})v(\vec{r}')\frac{\sin(q\,|\vec{r}-\vec{r}'|)}{q\,|\vec{r}-\vec{r}'|}d^3r d^3r' \\ &= 2\Delta f_0 \cdot (f_{0,R} - \rho_m V_R + f'_R(E)) \cdot \mathrm{Re}(A_0(q)A_R(q)), \end{aligned}$$

$$S_R(q,E) = |\Delta f_R(E)|^2 \iint\limits_{V_p} v(\vec{r})v(\vec{r}')\frac{\sin(q\,|\vec{r}-\vec{r}'|)}{q\,|\vec{r}-\vec{r}'|}d^3r d^3r' = |\Delta f_R(E)|^2\,|A_R(q)|^2\,. \tag{4}$$

Equations (4) give the non-resonant scattering, $S_0(q)$, the cross-term or mixed-resonant scattering, $S_{0R}(q,E)$, originating from the superposition of the scattering amplitudes of the non-resonant and the resonant scattering atoms and finally, $S_R(q,E)$, which contains the so-called pure-resonant scattering.

Measurement of scattering curves at three energies in the vicinity of the absorption edge of the atoms with atomic number Z constitutes the following vector equation:

$$\begin{aligned} &M_{ij}(E_i)\otimes A_j(q) = I_i(q,E_i)\\ &\begin{pmatrix} \Delta f_0^2 & 2\Delta f_0[\Delta f_{0,Z}+f'_Z(E_1)] & [(\Delta f_{0,Z}+f'_Z(E_1))^2+f''_Z(E_1)^2]\\ \Delta f_0^2 & 2\Delta f_0[\Delta f_{0,Z}+f'_Z(E_2)] & [(\Delta f_{0,Z}+f'_Z(E_2))^2+f''_Z(E_2)^2]\\ \Delta f_0^2 & 2\Delta f_0[\Delta f_{0,Z}+f'_Z(E_3)] & [(\Delta f_{0,Z}+f'_Z(E_3))^2+f''_Z(E_3)^2] \end{pmatrix} \begin{pmatrix} |A_0(q)|^2\\ \mathrm{Re}(A_0(q)A_R(q))\\ |A_R(q)|^2 \end{pmatrix}\\ &= \begin{pmatrix} I(q,E_1)\\ I(q,E_2)\\ I(q,E_3) \end{pmatrix}. \end{aligned} \tag{5}$$

When solving the vector Eq. (5) by the Gaussian algorithm (elimination procedure) the three basic scattering functions can be determined by the subsequent vector equation:

$$\begin{pmatrix} a_{11} & a_{12} & a_{13}\\ 0 & a_{22} & a_{23}\\ 0 & 0 & a_{33} \end{pmatrix} \begin{pmatrix} b_1\\ b_2\\ b_3 \end{pmatrix} = \begin{pmatrix} |A_0(q)|^2\\ \mathrm{Re}(A_0(q)A_R(q))\\ |A_R(q)|^2 \end{pmatrix}, \tag{6}$$

where the meaning of $a_{i,j}, b_j$ is published in more detail in [10], or in analytical form:

$$|A_R(q)|^2 = \left[\frac{I(q,E_1)-I(q,E_2)}{f'_Z(E_1)-f'_Z(E_2)} - \frac{I(q,E_1)-I(q,E_3)}{f'_Z(E_1)-f'_Z(E_3)}\right]\cdot\frac{1}{F(E_1,E_2,E_3)}, \tag{7}$$

where $F(E_1,E_2,E_3)$ represents a normalization factor composed of the anomalous dispersion corrections at the related three energies E_1,E_2,E_3 [11]. $|A_R(q)|^2$ is the pair correlation function of the resonant scattering atoms and thus represents the spatial distribution of the resonant scattering atoms. Due to Eq. (7) *ASAXS* provides a technique to access directly the small-angle scattering and by this the related structural information of the distribution of the Z-atoms. More generally spoken, Eq. (5) provides a method, which gives access to the pure-resonant scattering contribution of the selected constituent of a multi-component system by measuring the small-angle scattering at only three suitable energies [12,13].

From the matrix M'_{ij} of Eq. (6) the Turing numbers [14,15] of the three different systems (NaPA-solution with Sr^{2+} counter ions, SiGe-alloys and metallic glass of

$Ni_{68}, Nb_{16}Y_{16}$) have been calculated:

$$T(M') = \tfrac{1}{3} M' M'^{-1}$$
$$M' = \sqrt{\sum_{i,j=1}^{3} a_{ij}^2} \quad M'^{-1} = \sqrt{\sum_{i,j=1}^{3} b_{ij}^2}. \tag{6a}$$

From Eq. (6a) Turing numbers for the ASAXS measurements between 38 and 52 of the three systems have been found. Thus due to the Turing condition [15] accuracies clearly better than $\Delta I/I = 10^{-2}$ for the intensities of the scattering curves are required in order to allow for a matrix inversion, which yields significant basic scattering functions i.e. the error of the extracted basic scattering functions arising from error propagation through the inversion of the linear system of equations is small enough (see above).

From $|A_R(q)|^2$ and Eq. (6) the three basic scattering functions of Eq. (4) can be calculated analytically as is shown for the energies E_1 and E_2 as follows [12]:

$$\begin{aligned} S_R(q, E_1) &= |\Delta f_R(E_1)|^2 \cdot |A_R(q)|^2 \\ S_{0R}(q, E_1) &= (\Delta I(q, E_1, E_2) - S_R(q, E_1) + S_R(q, E_2)) \frac{(f_{0,R} - \rho_m V_R) + f'_R(E_1)}{f'_R(E_1) - f'_R(E_2)} \\ S_0(q) &= I(q, E_1) - S_{0R}(q, E_1) - S_R(q, E_1). \end{aligned} \tag{8}$$

The basic scattering functions, $S_{0R}(q, E)$, $S_0(q)$, carry important structural and quantitative information for instance the sign of the contrast between the nano-phases and the structure information of the non-resonant scattering component (see example).

3 ASAXS measurements on the distribution of Sr^{2+} counter ions around polyacrylate chains in highly diluted aqueous solution

3.1 Sample preparation and ASAXS measurements

The example focuses on the change in size and shape of sodium polyacrylate (NaPA) in aqueous solution, followed by the addition of alkaline earth cations. Alkaline earth cations are known to specifically interact with the anionic carboxylate residues, located on every other carbon atom of the polymer backbone. Formation of complex bonds between the anionic groups and alkaline earth cations neutralizes electric charges and thereby changes the nature of the respective chain segments. As a consequence, solubility of the polyelectrolyte is lowered which leads to a significant coil shrinking and eventually causes a precipitation of the respective alkaline earth salt [16,17]. Four solutions with the concentration between [NaPA] = 3.232 and 3.326 mM with ratios between $[Sr^{2+}]/[NaPA] = 0.451$ and 0.464 have been analyzed by ASAXS. The detailed description of the sample preparation (4 mm capillaries) is given in [13]. Here we focus on the separation of the form factor of the spatial distribution of the Sr^{2+} counter ions obtained from Eqs .(1)–(4) and the subsequent RI-analysis.

The ASAXS measurements were carried out at the JUSIFA beamline at HASYLAB, DESY Hamburg [7,8] using a double crystal (Si-311) monochromator with an energy resolution of about $\Delta E/E \approx 5 \cdot 10^{-5}$ covering a q-range between 0.075 and 2.5 nm^{-1} at three energies in the vicinity of the K-absorption edge of Sr at 16105 eV. The Sr-K-edge was measured from the solutions. From the change of the absorption coefficient the Sr-concentration of the solutions was confirmed. Figure 1 provides the anomalous dispersion corrections for Sr at the three energies used here based on the calculations of Cromer and Liberman [18,19].

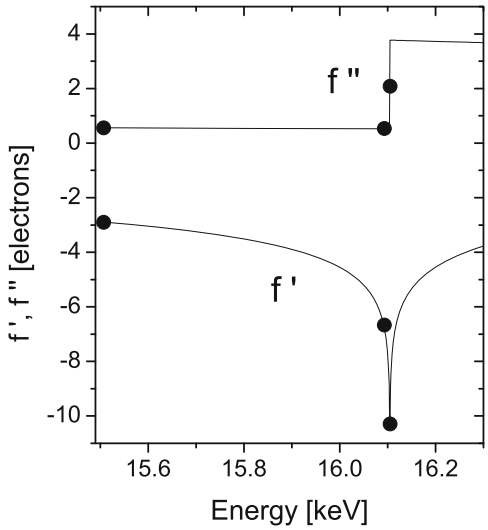

Fig. 1. Anomalous dispersion corrections of Sr [18,19].

3.2 Quantitative results from ASAXS measurements on diluted polyelectrolyte solutions

Figure 2 shows the total (black squares) and the separated (blue triangles) scattering curves and the form factor (red circles) of the Sr-counter ion distribution. The shape of the total scattering curve is compatible with the form factor of spherical objects, which is modulated by inter-spherical scattering contributions. The latter was already suggested by former SANS measurements [20]. This interpretation is strongly confirmed by the separated scattering curve (triangles) and the separated form factor (circles) of the Sr-ion distribution. Both curves exhibit a number of characteristic structures for $q > 0.1\,nm^{-1}$ with pronounced maxima, minima and shoulders revealing a scattering function, which is strongly influenced by correlation effects between rather monodisperse subdomains within the collapsing chains. Especially the form factor of the spatial distribution of the Sr-counter ions reveals a correlation maximum at $0.1\,nm^{-1}$. For a counter ion condensation-induced shrinking process such a model was first suggested by Rubinstein et al. [21] and was confirmed later by computer simulations [22–24]. The model, denoted as pearl-necklace, gives the scattering function of N spheres with radius R and with a distance d between the spheres.

In addition to the structural information, which can be obtained from $|A_R(q)|^2$, important quantitative information related to the amount of inhomogeneously distributed Sr-ions can be deduced from the integral Q_Z:

$$Q_Z(E) = |\Delta f_Z(E)|^2 \int_Q |A_R(q)|^2 \, d^3q. \tag{9}$$

In analogy to the so-called invariant [25], we will call $Q_Z(E)$ the Resonant Invariant (RI) of the inhomogeneously distributed resonant scattering Sr-ions. The Resonant Invariant, $Q_Z(E)$, as defined in Eq. (9), is related to the number density of inhomogeneously distributed Sr-ions, $\overline{v}_Z$, as was outlined in detail in previous publications

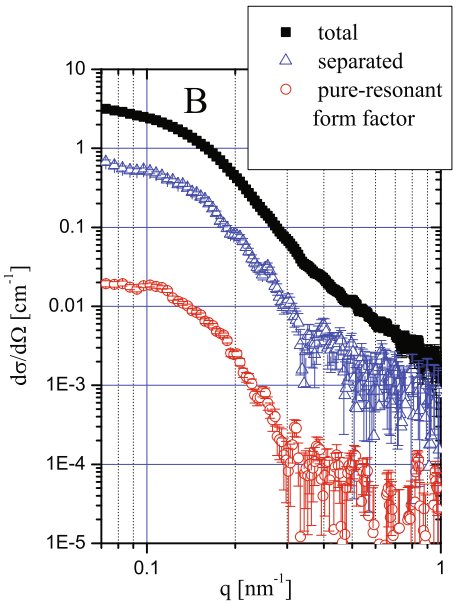

Fig. 2. Total scattering, separated scattering and the form factor of the pure-resonant scattering contribution of an aqueous polyacrylate solution with Sr-counter ions. The error bars have been calculated by error propagation of the statistical errors of the measured scattering curves.

[5,12,13]:

$$\overline{v_Z} = \frac{1}{2V_Z} \pm \sqrt{\frac{1}{4V_Z^2} - \frac{1}{(2\pi)^3 r_0^2} \int\limits_Q |A_R(q)|^2 d^3q}, \tag{10}$$

where $V_Z = 4\pi/3R_Z^3$ is the volume of the Z-atoms (here Sr^{2+}-ions) with ion radius R_Z and r_0 is the classical electron radius. In this presentation only one of the two solutions is significant i.e. the negative sign. Due to the integral Eq. (10) provides the quantitative analysis of chemical fluctuations independent of their structural distribution i.e. either in a two phase system or in short range order. It should be mentioned that the number density calculated from Eq. (10) includes the Z-atoms, which are homogeneously distributed in the solvent. These Sr-ions provide an isotropic scattering contribution at small q-values. As will be shown in more detail below, the amount of the isotropic scattering contribution originating from these remaining Sr-ions in the solvent can be neglected.

From the RI-analysis performed on ASAXS measurements of four samples with different ratios $[Sr^{2+}]/[NaPA]$ the concentrations of specifically interacting Sr^{2+}-ions were obtained (Table 1 and Fig. 3). Because the concentration of Sr-ions known from the compositions of the as-prepared solutions (and absorption measurements) amounts to $9 \cdot 10^{17}\,cm^{-3}$ only between 8.9 and 22.3% of the Sr-ions condensate on the polymer chain corresponding to values between $0.041 < r < 0.102$ of Sr-ions, which condensate per carboxylate macroion on the polymer backbone due to the ratios $0.451 < [Sr^{2+}]/[NaPA] < 0.464$. As can be seen from the inset in Fig. 3, the Sr-ions, which remain in the solvent, do not contribute significantly to the invariant in the q-regime under consideration and thus can be neglected.

Table 1. Structural and quantitative parameters of the four diluted Na-PA samples with different concentration ratios $[Sr^{2+}]/[NaPA]$ obtained from the ASAXS analysis. $\bar{v}$ represents the concentration of Sr-atoms in the condensed phase deduced from the experimentally accessible section of Resonant Invariant. Values of $\bar{v}^u$ represent the upper limits of these concentrations calculated with a theoretical model functions of the dumb bell for details see [13]. c is the relative amount of Sr-atoms in the condensed phase with respect to the total concentration of Sr-ions in the entire solution and r represents the ratio of Sr-cations to carboxylate side groups in the collapsed phase. Sample A represents an outlier possibly due to degradation of the sample. The latter was evidenced by LS-experiments showing strong differences of the radius of gyration taken before and after the ASAXS-measurements.

Sample	$[Sr^{2+}]/[NaPA]$	$\bar{v}$ $10^{17}[cm^{-3}]$	$\bar{v}^u$ $10^{17}[cm^{-3}]$	c[1)] [%]	r
A	0.464	0.77(14)	0.94	10.5	0.049
B	0.458	1.50(8)	1.92	21.4	0.097
C	0.4575	1.73(21)	2.01	22.3	0.102
D	0.451	0.73(12)	0.80	8.9	0.041

[1)]The values refers to $9.0 \cdot 10^{17}$ Sr^{2+} cations per cm^3 which correspond to 1.5 mM.

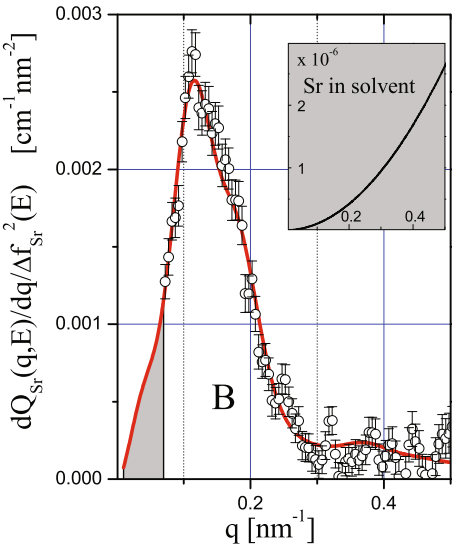

Fig. 3. The first derivative of the Resonant Invariant with upper integration limit q (Eq. (9)) of sample B. The model function was calculated in order to estimate the contribution of the missing scattering to the Resonant Invariant beyond the resolution of the ASAXS experiment (grey area on the left). The error bars have been calculated by error propagation.

4 Temperature induced differences in the nanostructure of hot-wire deposited silicon-germanium alloys analyzed by anomalous small-angle X-ray scattering

4.1 Sample preparation and ASAXS measurements

Hydrogenated amorphous silicon-germanium alloys are used in solar cell technology, where the germanium is added to produce lower band gap material to absorb the

longer wavelength photons of the solar spectrum and to achieve higher efficiencies in converting solar light into electrical energy. Previous small-angle X-ray scattering (SAXS) and anomalous small-angle X-ray scattering (ASAXS) studies revealed that, in addition to voids, non-uniformly distributed Ge contributes to the material inhomogeneities [26–29], which are strongly related to the degradation of the opto-electronic properties. In recent years there has been a growing interest especially in the hot-wire chemical-vapor depostion (HWCVD) technique [30] due to evidence of improved stability and improved opto-electronic properties of the material, as well as the potentially beneficial manufacturing feature of higher deposition rates than the current industrial technique of plasma-enhanced chemical vapor deposition (PECVD) [31,32].

A group at NREL (National Renewable Energy Laboratory, U.S.A.) found evidence of improved photoresponse from HWCVD a-SiGe:H alloys with narrow bandgaps deposited at different filament temperatures, filament diameters, and optimized substrate temperatures [33,34]. In what is to follow results from a series of six alloys a-Si_xGe_x : H (x = 0.6–0.69) deposited at different substrate temperatures between 130 and 360 °C are presented. The example demonstrates the determination of the amount of Ge located in mass fractals of 40 nm size employing the Resonant Invariant (RI) obtained from ASAXS measurements at the K-absorption edge of Germanium at 11.103 keV over an energy range of about 1 keV. Moreover from the Non-resonant Invariant (NI) the amount of voids was estimated depending on the substrate (deposition) temperatures. The correlation between the reduction of (hydrogen containing) voids and enhanced formation of (Ge containing) mass fractals explains the improvement of the photo conductivity of the materials at medium deposition temperatures by more than half an order of magnitude.

4.2 Quantitative results from ASAXS measurements on hot-wire deposited silicon-germanium alloys

Because the properties of the electronic contrast between the analyzed nano-phases were not clear (high in case of two phases of Si and Ge, low in case of slight concentration variations inducing a small Pivot-element [10]) the ASAXS measurements were extended over an energy range larger than 1 keV in order to reduce the Turing number as far as possible. Figure 4 shows the scattering curves of an alloy deposited at a substrate temperature of 305 °C. The blue triangles represent the pure-resonant scattering of the Ge-containing structures. The solid line passing through the blue symbols represent a fractal model function due to the Unified Exponential/Power Law Approach of Beaucage [35] giving evidence of Ge-containing mass fractals with a size of about 40 nm. Here the term mass fractal means, that the volume of the structure scales with R^D where D is the fractal dimension with $1 < D < 3$. Figure 5 summarizes the results obtained from RI- and NI-analysis at six different substrate temperatures. Figure 5(a) summarizes the results of the integrated pure-resonant scattering of the Ge component normalized to the total (known) amount of Ge i.e. $\overline{v_{Ge}}/n_{Ge}$. At lower temperatures (below 250 °C) only between 20 and 40% of the Ge-atoms are located in the mass fractals, while a dramatic change takes place at temperatures beyond, where more than 60% of the Ge-atoms are located in fractals. In parallel the analysis of the Non-resonant scattering contribution shows a reduction of hydrogen containing voids, when the substrate temperature is decreased (Fig. 5(b)). The blue triangles in Fig. 5(b) represent $\overline{v_H}/n_H$, which is the hydrogen quantity calculated from the

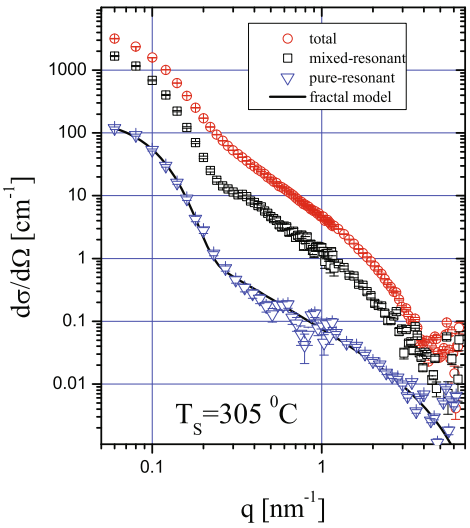

Fig. 4. Total scattering, separated scattering and the pure-resonant scattering contribution of Ge-containing inhomogeneities of a hotwire deposited hydrogenated SiGe-alloy (blue triangles). The solid line passing the blue triangles represent a mass fractal model function taken from [35].

Non-resonant scattering of Eq. (11) normalized to the known hydrogen content of the alloys n_H.

$$\overline{v_H} = \frac{1}{2V_H} - \sqrt{\frac{1}{4V_H^2} - \frac{1}{(2\pi)^3 r_0^2} \int\limits_Q |A_0(q)|^2 d^3q}. \tag{11}$$

Especially for the temperatures beyond 250 °C the ratio shows values which are far too high, i.e. 20, 40 and 60 times higher than expected from the hydrogen concentration. From this the conclusion can be drawn that the non-resonant scattering represents not only the scattering of hydrogen-filled inhomogeneities but also gives evidence for the existence of voids, which dominate the non-resonant scattering contribution. When the integral intensity of the non-resonant contribution is calculated in the q-range between 1 and 3 nm^{-1} (corresponding to structure sizes between 3 and 1 nm) the integral value reaches more than 50% of the value obtained from the overall integration, while the integration in the q-range between 0.06 and 0.2 (corresponding to structure sizes between 50 and 15 nm) shows only a weak dependence on the temperature with clearly lower values of $\overline{v_H}/n_H$. So one can conclude that the ratio $\overline{v_H}/n_H$ represents the ratio of voids to hydrogen atoms (i.e. the volume fractions) and that the non-resonant scattering contribution is clearly dominated by the scattering of voids with sizes of about several nm at higher substrate temperatures. These voids are strongly reduced when the substrate temperature is reduced and the optimum is reached, when the formation of the Ge mass fractals reaches a relative maximum in coincidence with a strongly reduced void fraction. The two processes cause the structural re-organization of Hydrogen from voids into Ge-fractals with enhanced Ge-H bonding, thereby improving the material photoconductivity. The latter was confirmed by IR-measurements indicating enhanced GeH bonding for these temperatures [33,34].

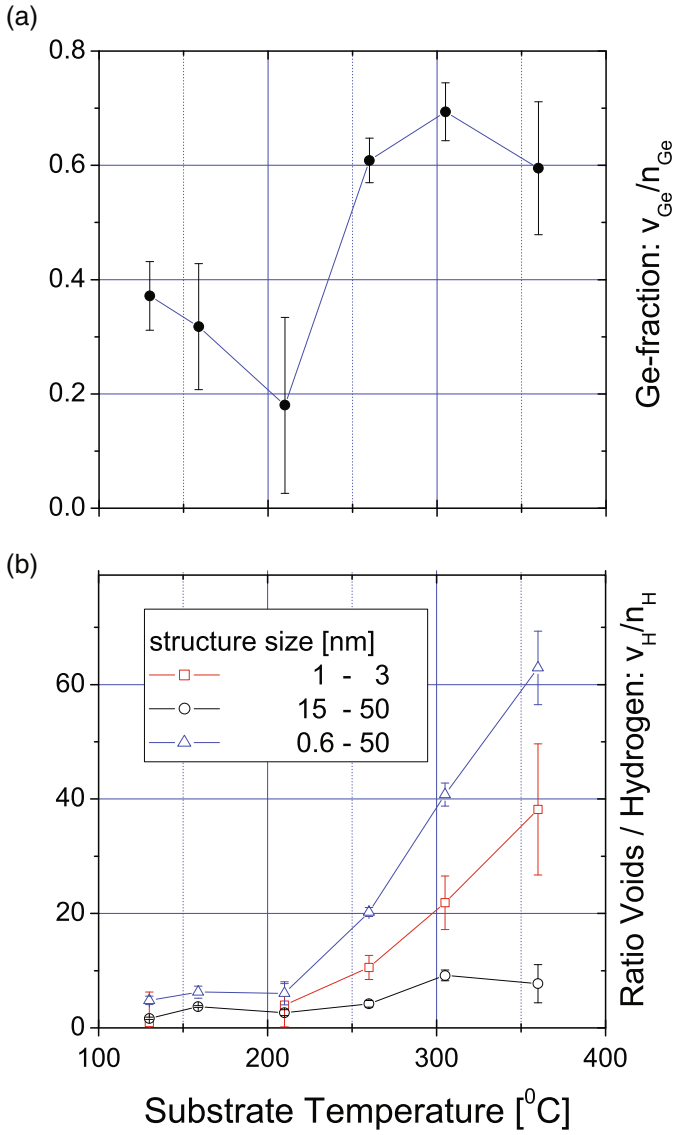

Fig. 5. The fraction of Ge-atoms implemented in the suggested fractal structure (a). The ratio of void scattering relative to the scattering expected from the hydrogen implemented in the amorphous matrix (b).

5 Spinodal decompostion of Ni-Nb-Y metallic glasses probed by quantitative anomalous small-angle X-ray scattering

5.1 Sample preparation and ASAXS measurements

The ternary Ni-Nb-Y system exhibits an extended miscibility gap in the liquid [36]. By means of rapid quenching technique the decomposed melt can be frozen into a phase separated metallic glass [37]. The critical temperature of liquid-liquid decomposition depends on the composition. For Ni content <60 at% a hierarchical heterogeneous microstructure is obtained with size distribution from 10 nm up to 500 nm which can

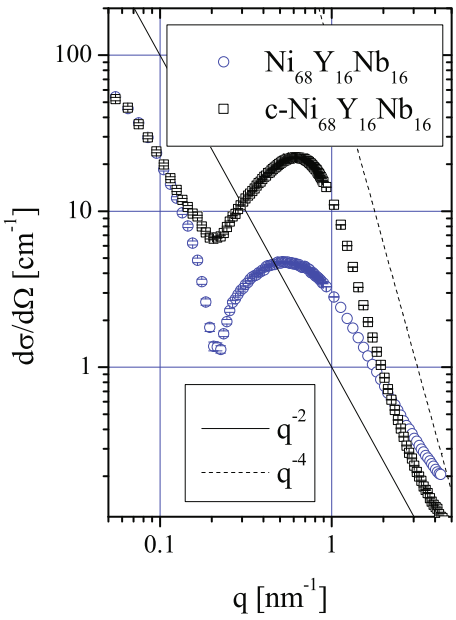

Fig. 6. Total scattering curves of the alloy $Ni_{68}Nb_{16}Y_{16}$ with different heat treatments: as-quenched (blue circles) and heat-treated above the first crystallization point at 773 K but below the second crystallization point (black squares). Above the first crystallization point the asymptotic behavior of the scattering curves changes from q^{-2} to q^{-4}, indicating smooth interfaces probably between the small crystallites and the surrounding amorphous phase.

be analyzed by transmission electron microscopy (TEM). Such microstructures represent a coarsened state of spinodal decomposition, growth of the melts, and secondary decomposition within the liquids. For such phase separated Ni-Nb-Y glasses SAXS curves with fractal q-dependence have been observed [38]. For alloys with Ni > 60 at% early stages of phase separation can be obtained due to reduced critical temperature having fluctuation in nm dimensions with almost no contrast in TEM images. By means of ASAXS quantitative parameters of the fluctuation can be determined.

In the following results from a sample with the composition $Ni_{68}Nb_{16}Y_{16}$ are presented. The sample was prepared by single-roller melt spinning under argon atmosphere. The casting temperature was 1923 K. Details of samples preparation are published in [36]. Additionally, a partly crystallized sample, c-$Ni_{68}Nb_{16}Y_{16}$, was produced by heating part of the ribbons in a differential scanning calorimeter (DSC 7, Perkin Elmer) just above the temperature of the first exothermic crystallization event at 773 K over 30 min.

ASAXS sequences were performed for both samples with four X-ray energies in the vicinity of the K-absorption edges of Nickel at 8333 eV, Yttrium at 17038.4 eV and Niobium at 18985.6 eV. For the three very different energy ranges nearly the same q-range was covered.

5.2 Quantitative results from ASAXS measurements on Ni-Nb-Y metallic glasses

The influence of partial crystallization on the SAXS curves is shown in Fig. 6 by the comparison of the scattering curves of the two alloys. Both samples show a correlation maximum corresponding to a correlation length of 12.2 nm, which represents the spatial extension (wavelength) of the concentration fluctuations respective in case of the

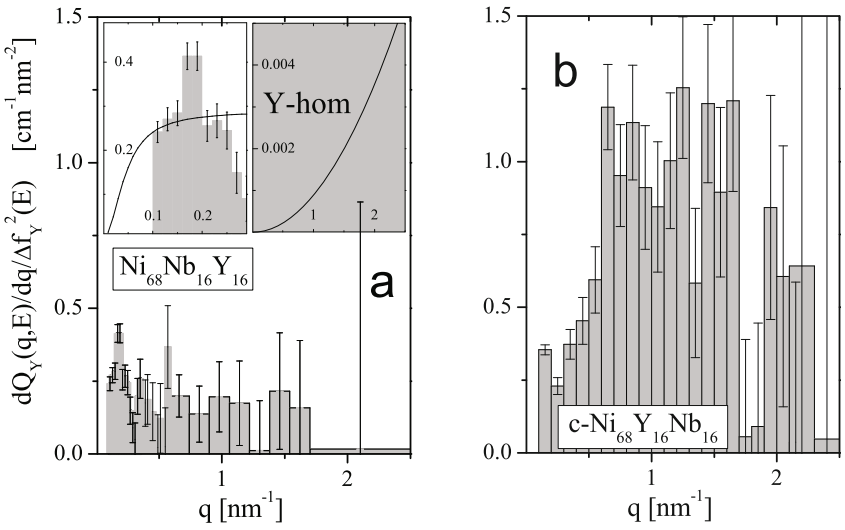

Fig. 7. The first derivative of the resonant invariant (Eq. (9)) of (a) as-quenched and (b) partially crystallized $Ni_{68}Nb_{16}Y_{16}$ obtained from ASAXS sequences at the Y K-edge (17038 eV). The integrals (grey area) represent the resonant invariant from which the Y concentrations can be calculated. The right inset represents the upper limit of 16 at.% homogeneously distributed Y, contributing to the resonant invariant. The left inset explains the contribution that is missing due to the q-resolution.

partially crystallized sample the distance between the crystallized domains. The heat treated sample consists of a nanocystalline Ni_2Y phase and a remaining amorphous Ni-Nb phase. In the SAXS curves a dramatic change takes place for the sample, which was heat treated beyond the 1st crystallization temperature. Though the correlation maximum remains unchanged on the q-axis, it is shifted on the y-axis by nearly an order of magnitude probably due to a higher electron density contrast caused by a larger concentration gradient. Additionally the asymptotic behaviour changes from q^{-2} to q^{-4} indicating the formation of small crystallites with smooth interfaces to the surrounding phase. Obviously the fluctuation length of the as-quenched state determines the size of the nanocrystals. Because the Nickel component serves as the matrix, the important quantitative parameters of decomposition are related to the concentration fluctuations of Yttrium and Niobium and thus have been obtained from quantitative ASAXS measurements at the K-absorption edges of Yttrium and Niobium.

Figure 7 shows the first derivative of the Resonant Invariant for Yttrium of the as-quenched sample (a) and the crystallized sample (b). The grey areas represent the integrals, Q_Z (i.e. the Resonant Invariant), which are introduced into Eq. (9) for the calculation of the amount of Yttrium atoms, $\overline{v}_Y$, which enter the concentration fluctuations of the as-quenched sample and the crystallites of the heat-treated sample respectively. From Eq. (9) an amount of $2.13(28) \cdot 10^{21}\,\mathrm{cm}^{-3}$ Yttrium (excess) atoms, which enter the crystallites, was calculated corresponding to about 19% of the Y-atoms in the alloy.

A completely different result was obtained from the analysis of the Resonant Invariant of the as-quenched sample. As can be seen already from a simple comparison of the integrals of both samples in Fig. 7, the amount of Yttrium atoms, which enter the concentration fluctuations must be much more smaller. From Eq. (9) a concentration of $0.39(20) \cdot 10^{21}\,\mathrm{cm}^{-3}$ Yttrium atoms was deduced, which corresponds to an amount of only 4% Yttrium atoms.

Though this result is significant, it is near the resolution limits of the experiment as can be seen from the error bars in Fig. 7(a). For a more quantitative discussion of the result, the limited integration area has to be extended onto the whole regime $0 \leq q < \infty$. Because no comprehensive description of the scattering curves of a ternary alloy undergoing spinodal decomposition is at hand, a model function with a q^{-2}-behaviour (Ornstein-Zernike originally for binary systems) was employed. The model function serves only as a guide for the eye with the aim to estimate the amount of the 'missing' scattering contributions at higher and lower q-values i.e. beyond the resolution of the experiment (left inset in Fig. 7(a)).

At $q = 0$ the model function reaches a finite value defined by thermodynamic parameters of the alloy and the first derivative of the Resonant Invariant approaches 0 with $q \to 0$. The amount of missing contribution to the Resonant Invariant can be neglected as can be seen from the left inset in Fig. 7(a), which shows a magnified part of the Resonant Invariant in the low q-range. The missing part below the resolution at q-values smaller $q_{\min}$ is the area between the grey histogram and the solid line of the model function.

The right inset in Fig. 7(a) represents the contribution of homogeneously distributed Y-atoms with a concentration of 16at% to the Resonant Invariant. Although this corresponds to the maximum possible amount – a considerable portion of the Y-atoms are localized in the fluctuations – the contribution is many orders of magnitude smaller than the contribution detected from the Y-atoms in the concentration fluctuations and thus can be also neglected.

Considering the scattering contributions beyond the q-resolution at higher q-values the result must be interpreted as a lower limit as is demonstrated by of the model function (Fig. 7(a)). At higher q-values a cut-off of the scattering function is expected, because otherwise the integral of Eq. (9) would become infinite and the invariant would not exist. As can be seen from Fig. 7(a) the cut-off of the pure-resonant contribution cannot be resolved due to the large error bars (at $2\,\mathrm{nm}^{-1}$ the error bar is more than an order of magnitude larger compared to the value) and if the cut-off is located at q-values beyond $2\,\mathrm{nm}^{-1}$, the concentration of Yttrium atoms must be higher. An extension of the upper integration limit to $q_{\max} = 15\,\mathrm{nm}^{-1}$, which roughly corresponds to the nearest neighbor atomic distance cannot provide additional significant contributions. On the other hand recent atom probe measurements on similar alloys $Ni_{66}Nb_{17}Y_{17}$ [39] have confirmed the quantitative results of the RI-analysis outlined in this paper. In the case of the crystallized sample the scattering curve at larger q-values is deep in the Porod regime and no significant contribution can appear in the integral at higher q-values. Similar results were deduced for Niobium from RI-anaylsis at the K-absorption edge of Niobium.

6 Conclusion

In the last years Anomalous Small-Angle X-ray Scattering became a precise quantitative method for element specific structural analysis on the mesoscopic length scale. Due to the precision of the techniques small-angle scattering contributions in the resolution regime $10^{-3} < \Delta I/I < 10^{-2}$ can be reliably separated and the pure-resonant scattering of numerous multi-component systems becomes accessible for quantitative analysis.

The pure-resonant scattering contributions (1) of a diluted chemical solution of negatively charged polyacrylates surrounded by divalent Sr-counter ions, (2) of hydrogenated semiconductor alloys and (3) of metallic glasses one of them in the state of spinodal decomposition have been analyzed quantitatively. From the calculation of the Resonant Invariant (RI) the amount of Sr-ions localized in the partially collapsed

sub-domains of polyacrylate colloids was deduced. From the RI-analysis of hotwire deposited hydrogenated Silicon-germanium alloys the amount of Germanium atoms located in 40 nm sized mass fractals was determined. Moreover from the analysis of the Non-resonant Invariant (NI-analysis) the structural reorganization of hydrogen from voids into mass fractals was deduced. The latter could be correlated to enhanced photo conductivity of the semiconductor alloy. In a 3rd example the amount of Y-atoms located in concentration fluctuations with a correlation length of 15 nm were determined by RI-analysis and compared to an alloy of the same composition, after heat treatment causing partially re-crystallization.

References

1. J.P. Simon, J. Appl. Cryst. **40**, 1 (2007)
2. F.B. Rasmussen, A.M. Molenbrock, B.S. Clausen, R. Feidenhans'l, J. Catalysis **190**, 205 (2000)
3. A. Bota, Z. Varga, G. Goerigk, J. Phys. Chem. C **112**, 4427 (2008)
4. D. Tatchev, A. Hoell, M. Eichelbaum, K. Rademann, Phys. Rev. Lett. **106**, 085702-1 (2011)
5. G. Goerigk, N. Mattern, Acta Materialia **57**, 3652 (2009)
6. M. Patel, S. Rosenfeldt, M. Ballauff, N. Dingenouts, D. Pontoni, T. Narayanan, Phys. Chem. Chem. Phys. **6**, 2962 (2004)
7. H.-G. Haubold, K. Gruenhagen, M. Wagener, H. Jungbluth, H. Heer, A. Pfeil, H. Rongen, G. Brandenburg, R. Moeller, J. Matzerath, P. Hiller, H. Halling, Rev. Sci. Instrum. **60**, 1943 (1989)
8. G. Goerigk 'Electronic and Computer Upgrade at ASAXS Beamline JUSIFA', HASYLAB Annual Report (2006), p. 77
9. H.B. Stuhrmann, Adv. Polymer Science **67**, 123 (1985)
10. G. Goerigk, N. Mattern, J. Phys. Conf. Ser. **247**, 012022 (2010)
11. G. Goerigk, R. Schweins, K. Huber, M. Ballauff, Europhys. Lett. **66** 331 (2004)
12. G. Goerigk, D.L. Williamson, J. Appl. Phys. **99**, 084309 (2006)
13. G. Goerigk, K. Huber, R. Schweins, J. Chem. Phys. **127**, 154908 (2007)
14. J. Westlake, A Handbook of Numerical Matrix Inversion and Solution of Linear Equations. (New York: J. Wiley and Sons, 1968)
15. J.P. Simon, O. Lyon, D. de Fontaine, J. Appl. Cryst. **18**, 230 (1985)
16. I.J. Michaeli, Polym. Sci. **48**, 291 (1960)
17. K. Huber, J. Phys. Chem. **97**, 9825 (1993)
18. D.T. Cromer, D. Liberman, J. Chem. Phys. **53**, 1891 (1970)
19. D.T. Cromer, D. Liberman, Acta Cryst. **A37**, 267 (1981)
20. R. Schweins, P. Lindner, K. Huber, Macromolecules **36**, 9564 (2003)
21. A.V. Dobrynin, M. Rubinstein, S.P. Obukhov, Macromolecules **29**, 2974 (1991)
22. U. Micka, Ch. Holm, K. Kremer, Langmuir **15**, 4033 (1999)
23. P. Chodanowski, S. Stoll, J. Chem. Phys. **111**, 6069 (1999)
24. H.J. Limbach, Ch. Holm, J. Phys. Chem. B **107**, 8041 (2003)
25. O. Glatter, O. Kratky, Small-Angle X-ray Scattering (Academic Press, London, 1982)
26. D.L. Williamson, Mater. Res. Soc. Symp. Proc. **377**, 251 (1995)
27. G. Goerigk, D.L. Williamson, Solid State Commun. **108**, 419 (1998)
28. G. Goerigk, D.L. Williamson, J. Non-Cryst. Solids **281**, 181 (2001)
29. G. Goerigk, D.L. Williamson, J. Appl. Phys. **90**, 5808 (2001)
30. E.C. Molenbroek, A.H. Mahan, A. Gallagher, J. Appl. Phys. **82**, 1909 (1997)
31. B.P. Nelson, Y. Xu, D.L. Williamson, B. von Roedern, A. Mason, S. Heck, A.H. Mahan, S.E. Schmitt, A.C. Gallagher, J. Webb, R. Reedy, Mat. Res. Soc. Symp. Proc. **507**, 447 (1998)
32. B.P. Nelson, Y. Xu, D.L. Williamson, D. Han, R. Braunstein, M. Boshta, and B. Alavi, Thin Solid films **430**, 104 (2003)

33. Y. Xu, B.P. Nelson, D.L. Williamson, L.M. Gedvilas, and R.C. Reedy, Mat. Res. Soc. Symp. Proc. **762**, A 10.2 (2003)
34. Y. Xu, B.P. Nelson, L.M. Gedvilas, R.C. Reedy, Thin Solid Films **430**, 197 (2003)
35. G. Beaucage, J. Appl. Cryst. **28**, 717 (1995)
36. N. Mattern, M. Zinkevich, W Löser, G Behr, J.J. Acker, Phase Equil. Diff. **29** 141 (2008)
37. N. Mattern, U. Kühn, A. Gebert, T. Gemming, M. Zinkevich, H. Wendrock, L. Schultz, Scripta Materialia **53**, 271 (2005)
38. N. Mattern, T. Gemming, G. Goerigk, J. Eckert, Scripta Mater. **57**, 29 (2007)
39. A. Shariq, N. Mattern, Ultramicroscopy **111**, 1370 (2011)